Fast Magnetic Micropropellers with Random Shapes

Peter J. Vach,[†] Peter Fratzl,[†] Stefan Klumpp,[‡] and Damien Faivre[*,†]

[†] Department of Biomaterials and [‡] Department of Theory and Bio-Systems, Max Planck Institute of Colloids and Interfaces, Science Park Golm, 14424 Potsdam, Germany

*Corresponding author's email: damien.faivre@mpikg.mpg.de.

Supporting information

1. Methods

Synthesis of magnetic microppellers. The synthesis method for the production of the carbon coated magnetic nanostructures has been described previously[1]. Briefly, magnetic iron oxide nanoparticles (NanoArc iron(III) oxide, Alfa Aesar) are suspended in a glucose solution and heated to 180 °C for 24 h. The iron oxide catalyzes the thermal decomposition of the glucose, leading to the deposition of a carbon layer on the iron oxide nanoparticles[2-4]. In this way, aggregates of magnetic nanoparticles are structurally fixed. Reaction products are washed several times with ethanol and de-ionized water, using magnetic separation, and are used without further processing.

Speed measurements. Speeds were measured at the lower surface of a glass capillary (0.2 × 2 × 50 mm, Vitrotubes, Vitrocom). As-synthesized magnetic nanostructures were filled into the capillary, which was subsequently placed in the microscope sample holder with the actuating magnetic field off. After all structures had settled to the lower capillary surface, the actuating field was switched on and a video of the lower capillary surface was recorded immediately afterwards in the center of the capillary. After one such measurement the capillary was discarded, since the application of an actuating magnetic field destroys the random initial distribution of structures in the capillary. The concentration of the structures was adjusted to an intermediate range, high enough so that many propellers (on average around 17)

could be characterized in one measurement, but low enough to avoid frequent hydrodynamic or magnetic interactions between the structures. The recorded videos were analyzed by manually searching for start and end positions, in between which a structure moved undisturbed by any other structure. The movement parallel to the vector of rotation of the actuating field was interpreted as propulsion, whereas the movement perpendicular to the propeller was interpreted as rolling movement (Figure S1). Although this measure of propulsion speed is not in general equivalent to the propulsion speed in bulk liquid, far away from a surface (see SI), it has established as a standard technique to measure propulsion speeds[5,6,7]. For the present study, it was in particular necessary to use this method for measuring the propulsion speed, in order to allow the measured speeds to be compared to those of previously reported magnetic propellers. The size of the structure was determined by searching for a frame in which the propeller appeared in focus, as well as in the orientation that leads to the biggest 2D projection. The distance was then determined manually by measuring the distance between the most distant pixels in the 2D projection (see inset in Figure S1 a). Videos were recorded for a duration of 59.22 s. This finite measurement time leads to a bias, since faster propellers have a higher chance of reaching the field of view during that time (and thus being measured) than slow propellers. We performed a self-consistency check by simulating the experimental procedure in order to show that this bias can be neglected (see SI).

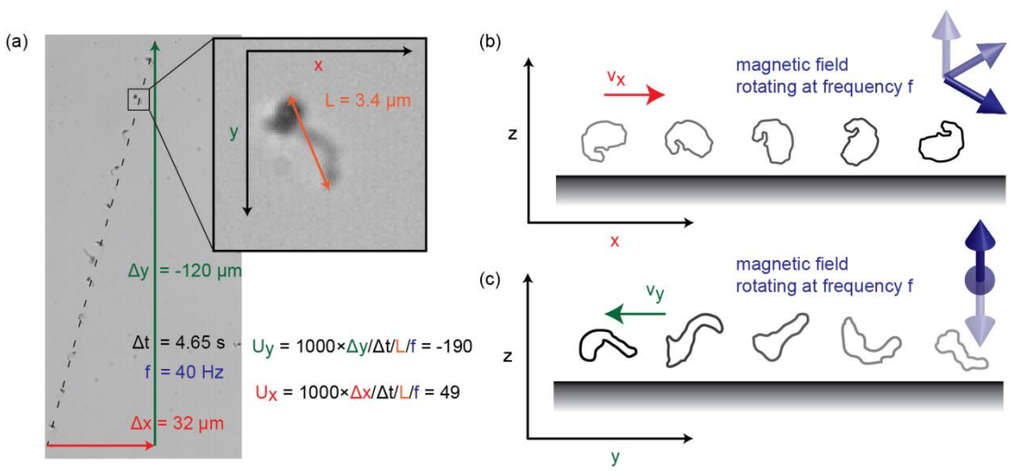

Figure S1: Schematic explanation of measurements of dimensionless speeds. (a) The dashed black line indicates the trajectory of a propeller. Images of the propeller after time steps of 0.42 s are superimposed on the initial frame to create a time-lapse image. In total the propeller traverses a distance of 120 µm in negative y direction and 32 µm in positive x direction during a time $\Delta t = 4.65\ s$. Speeds were measured by noting start and end positions and the time difference. The view in which the propeller appears biggest is magnified in an inset. The propeller size was always measured for the view (angle) in which the propeller appeared biggest when in focus. Based on these measurements the dimensionless propulsion speeds (U_y) and dimensionless rolling speeds (U_x) were calculated for all propellers in the dataset. (b) The rolling motion is due to the fact that the propellers are imaged close to a glass surface, towards which they are pulled by gravity. The shearing of water close to the glass and propeller surfaces mediates a friction that results in a rolling motion[8,4]. The arrow of time is indicated in this schematic by a darkening of shape outlines and magnetic field vectors. (c) Since the propellers typically have a finite rotation-translation

coupling, they propel parallel or anti-parallel to the vector of rotation of the actuating magnetic field. The arrow of time is again indicated by a darkening of shape outlines and magnetic field vectors.

The 3D shape of magnetic micropropellers can be reconstructed by an optical tomographic technique. We recorded the videos at 50 frames per second, whereas the actuating frequency f was either 10, 20 or 40 Hz. Therefore, video images contain five distinct projections for each measured aggregate (Figure S2). The actuating frequency was sufficiently low, so that the aggregates could follow the magnetic field. Before reconstruction, we checked the assumption that the structure rotates with the actuating frequency explicitly, by comparing frame n with frame n+5. The structures could be reconstructed if their size was big enough, so that important features are visible in the optical microscope, but small enough, so that the complete structure was approximately in focus for every orientation. Images of suitable aggregates were selected and the 2D projections of the aggregate were manually outlined. The thus defined 2D projections were projected into a voxel cube at appropriate angles. Offsets were estimated based on the movement of the structure from frame n to frame n+5. Voxels that were hit by all five projections formed the initial reconstructed 3D shape. This initial reconstruction was then refined by searching for offset values that maximized the number of voxels in the reconstructed 3D shape, using discrete optimization (see SI). Finally, the reconstructed 3D shape was projected back to 2D for the visual verification of the reconstruction. If all prominent features of the original images were also present in the images reprojected from the reconstruction, we deemed the reconstruction successful. 47 out of 55 attempted reconstructions were successful. The reconstruction method is schematically explained in Figure S2.

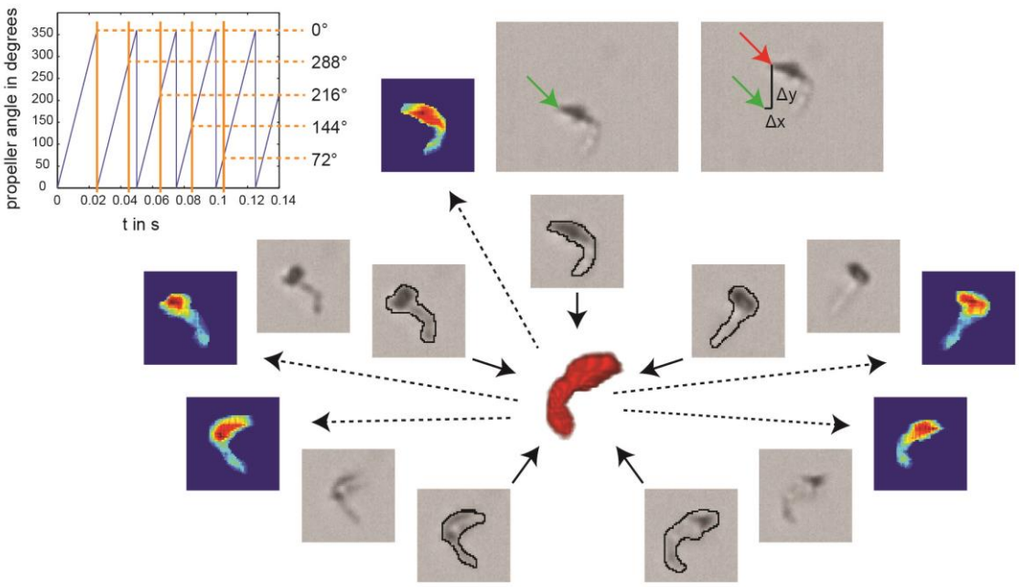

Figure S2: Schematic explanation of the reconstruction method. In this example the propeller rotates with 40 Hz, and the images were recorded with 50 frames per second. As can be seen in the plot on the top left, this results in images being taken from 5 distinct angles (0°, 72°, 144°, 216°, 288°). After 0.12 s, the angle is again the same as at t = 0 s, however the propeller has moved by $\Delta y \approx 2.5$ µm and $\Delta x \approx 0.4$ µm (top right). The five images of the propeller are manually outlined. The area inside the outline is then projected into a voxel cube at the correct angle. The projections are offset against each other initially by $\Delta x/6$ and $\Delta y/6$. The voxels that are hit by all five projections become part of the initial reconstructed 3D shape. In the next step, discrete optimization is used to find parameters $\Delta\tilde{x}$ and $\Delta\tilde{y}$, which maximize the number of voxels in the reconstructed 3D shape. Finally, the optimized reconstructed 3D shape is projected back to 2D at the correct angles. The resulting color coded projections are displayed next to the original images. The color code implies how many voxels of the final 3D reconstructed shape were mapped to one pixel in the 2D projection (from none (blue) to many (red)). These projections are then compared to the original images. If all discernible features in the original image are also present in the reconstruction, the reconstruction is deemed successful.

Equipment. Videos of propeller motion were recorded using a high-speed camera, controlled by software provided by the camera manufacturer (Timebench, Optronis). The magnetic fields were generated by a 3D Helmholtz coil system (C-SpinCoil-XYZ, Micro Magnetics Inc.). The Helmholtz coils are arranged around the sample holder of a custom made microscopy setup described previously[9].

2. Estimate of the Reynolds number

The Reynolds number of an actuated nanostructure can be estimated as follows. Assuming $L < 2 \times 10^{-5}$ m, a rotation frequency $\omega < 200$ Hz and a liquid medium of water at room temperature (20 °C), the Reynolds number can be calculated:

$$Re < \frac{2 \times 10^{-5}\ \mathrm{m}}{10^{-3}\ \mathrm{N\ m^{-2}\ s}} \times 10^{3}\ \mathrm{kg\ m^{-3}} \times 2\pi \times 200\ \mathrm{s^{-1}} \times 10^{-5}\mathrm{m} = 2.5 \times 10^{-1} \ll 1 \quad \text{(S1)}$$

The Stokes equations are thus indeed suited for the hydrodynamic description of magnetic micropropellers.

3. Proof that the rotational friction coefficient is always positive.

As noted in the main text the symmetric and positive definite matrix $\mathbf{P}$ is called the resistance matrix[10]. In general it is a 6×6 matrix, but in the main text it is only 2×2. This is because there F, τ, v and ω_p are scalar quantities, since the propeller must move on average parallel to the rotation axis for symmetry reasons. The discussion in the main text is thus a reasonable simplification that ignores movement on timescales $t < 1/\omega_p$. A and D are related to translational and rotational friction respectively. C describes the coupling between rotation and translation. $\mathbf{P}$ being positive definite implies:

$$LAa^2 + L^3Db^2 > -2L^2Cab \tag{S2}$$

for arbitrary real numbers a and b. It follows that $A > 0$ and $D > 0$. Assuming $Cab < 0$ equation S2 can be rewritten as:

$$\frac{Aa^2}{L^2 4b^2} + \frac{D}{2} + \frac{L^2D^2b^2}{4Aa^2} > \frac{C^2}{A} \tag{S3}$$

Since particular a and b that simultaneously satisfy $\frac{Aa^2}{L^2 4b^2} + \frac{L^2D^2b^2}{4Aa^2} = \frac{D}{2}$ and $Cab < 0$ can always be found $\left(\frac{a^2}{b^2} = \frac{DL^2}{A}\right)$, equation S3 implies:

$$D > \frac{C^2}{A} \tag{S4}$$

Therefore the quantity $c_F = \eta L^3 (D - C^2/A)$ is always positive.

4. Comparison to previously published propellers.

In Figure 3, we compare the dimensionless speed of previously published propeller designs to the observed distribution of dimensionless speeds for random structures. In Figure S3 we reproduce images of the previously published propeller designs used in this comparison. The speeds of the previously reported propellers might have been artificially enhanced in some cases, by not differentiating between rolling and propulsion speeds. Furthermore, although it seems that all propeller speeds were measured close to a solid surface, some papers do not explicitly report that. If these propellers would have been actuated in bulk, their speed is increased relative to our measuring method (see Figure S8). Thus the values we use for comparison are upper limits on the performance of previous propeller designs when actuated in the experimental conditions used in this paper, except for the propellers in Figure S3 panels c and g, which were not actuated in water.

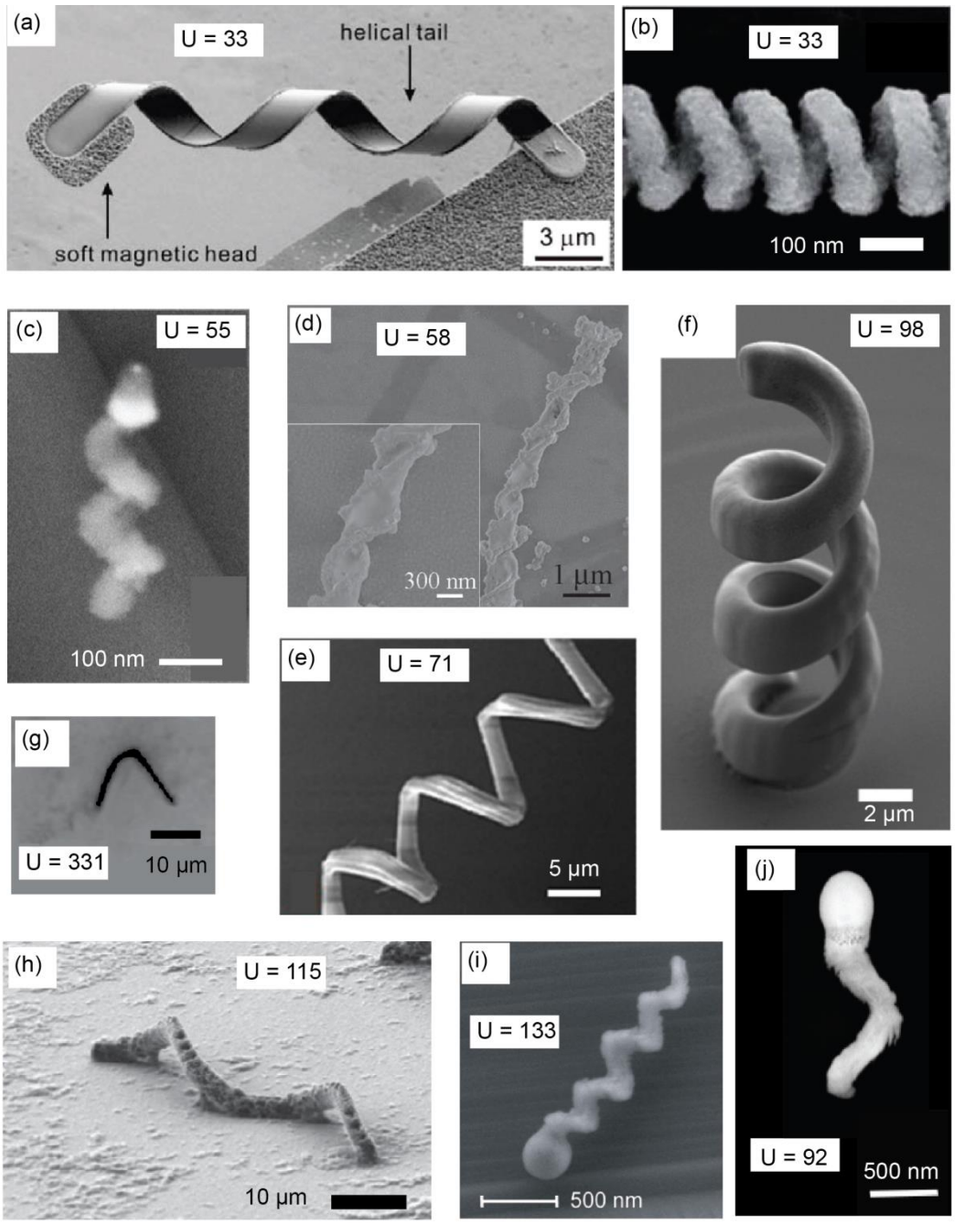

Figure S3: Comparison of dimensionless speed values for different propeller designs. The speed measurements reported here were all done in water close to a solid interface, except for (c) which was measured in 3 mg/ml viscoelastic hyaluronan solution and (i) which was measured in a high density 0.5 µm-diameter microbead solution. (a) Micropropeller made from self-scrolling thin films[5]. Scale bar: 3 µm. $U \approx 10^3 \frac{8\ \mu m s^{-1}}{38\ \mu m\ 10\ Hz} = 33$. Adapted with permission from[5]. Copyright 2009 ACS. (b) Nanopropeller from template electrosynthesis [11]. Scale bar: 100 nm. $U \approx 10^3 \frac{15 \mu m s^{-1}}{3 \mu m\ 150\ Hz} = 33$. (Not clear if rolling and propulsion have been separated). Adapted from [11] with permission from The Royal Society of Chemistry. (c) Extremely small nanopropeller made using glancing angle vapor deposition (GLAD) [12]. Scale bar: 100 nm. $U \approx 10^3 \frac{1.1\ \mu m s^{-1}}{0.4\ \mu m\ 50\ Hz} = 55$. Adapted with permission from [12]. Copyright 2014 ACS. (d) Micropropeller produced using helical lipid microstructures [13]. Scale bars are 300 nm (inset) and 1 µm. $U \approx 10^3 \frac{0.41\ \mu m s^{-1}}{11.8\ \mu m\ 0.6\ Hz} = 58$. (Not clear if rolling and propulsion have been separated). Adapted with permission from [13]. Copyright 2012 Wiley-VCH. (e) Micropropeller based on spiral xylem vessels [14]. Scale bar: 5 µm. $U \approx 10^3 \frac{250\ \mu m s^{-1}}{50\ \mu m\ 70\ Hz} = 71$. (Not clear if rolling and propulsion have been separated). Adapted with permission from [14]. Copyright 2013 ACS. (f) Micropropeller fabricated using direct laser writing (DLW) [7]. Scale bar: 2 µm. $U \approx 10^3 \frac{86\ \mu m s^{-1}}{35\ \mu m\ 25\ Hz} = 98$. Adapted with permission from [7]. Copyright 2012 Wiley-VCH. (g) Scheme of a micropropeller based on magnetically assembled curved nickel nanowires as in [15]. A scale bar is presented as guide for the eye: 10

µm. $U \approx 10^3 \frac{10.6\ \mu m s^{-1}}{16\ \mu m\ 2\ Hz} = 331$. (h) Micropropeller fabricated by direct laser (DLW) writing of photoresist containing superparamagnetic nanoparticles aligned by an external magnetic field [16]. Scale bar: 10 µm. $U \approx 10^3 \frac{28.2\ \mu m s^{-1}}{60\ \mu m\ 4.1\ Hz} = 115$. (Differentiates rolling and propulsion.) Adapted with permission from [16]. Copyright 2014 Wiley-VCH. (i) Nanopropeller made using GLAD [6]. Scale bar: 500 nm. $U \approx 10^3 \frac{40 \mu m s^{-1}}{2 \mu m\ 150\ Hz} = 133$.(Rolling seems negligible, but maybe rolling and propulsion were not seperated). Adapted with permission from [6]. Copyright 2009 ACS. (j) Optimized nanopropeller made using GLAD [17]. Scale bar: 500 nm. $U \approx 10^3 \frac{7.89\ \mu m s^{-1}}{1.45 \mu m\ 59.4\ Hz} = 92$. (reported speed is parallel to axis of rotation) Adapted with permission from [17]. Copyright 2015 ACS.

5. Simulation of measurement procedure.

In order to increase the number of dimensionless speeds that could be measured in an experiment, structures which entered or left the field of view during the measuring time of 59.22 s were counted as well. As noted in the main text, the dimensionless speeds of random structures were measured in the center of the capillary. This was done to avoid bias, as otherwise more propellers would be available to reach the field of view from above or below.

However, the finite measurement time does lead to a bias, since faster propellers have a higher chance of reaching the field of view during that time (and thus being measured) than slow propellers. In order to check if this bias is significant, a self-consistency check was performed by simulating the experimental procedure. The measured distributions of dimensionless speeds were assumed as true values in the simulation and the simulated measurement results were compared to the assumed true speed distributions (Figure S4). The simulations show that the choice of a measurement time of 59.22 s does not lead to large changes in the measured distributions. After the actuating field is switched on, the control electronics take about 10-20 s to establish a stable field. The total measurement time could thus be higher, but even measurement times of about 90 s, do not significantly change the distribution of propulsion speed. No attempt was made to numerically remove the small but existing bias effect, since it is not clear if the finite measurement leads to an over- or underestimation of the propulsion speed standard deviation. This is due to the fact that, for long measurement times, the initial effect of faster propellers being more likely to reach the field of view, is counteracted by the depletion of fast propellers above and below the field of view (see Figure S4 d).

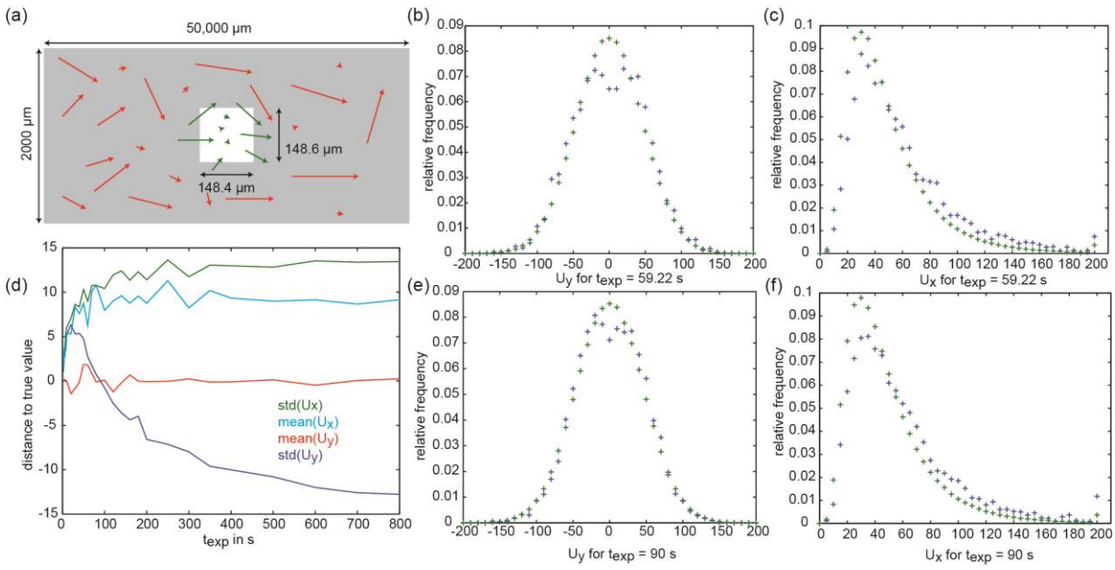

Figure S4: Simulation of speed measurement, to check for consistency. (a) Schematic of the experimental setup (sizes not to scale). The capillary (grey) is much bigger than the field of view (white square). Arrows indicate possible propeller movements during the simulated measurement time t_{exp}. Some propellers cross the field of view and their speed is measured (green arrows) others not (red arrows). The fact that faster propellers can reach the field of view more quickly leads to a bias. To investigate this bias the measurement was simulated, by drawing propeller properties from random distributions (Gaussian for U_y, log-normal for U_x) modeled on the measured distributions. (b) Histograms of U_y in a simulated measurement with measurement time $t_{exp} = 59.22$ s. The green crosses mark the assumed true distribution for U_x, whereas the blue crosses mark the distribution that would be measured on average (based on 1 million sample propellers). (c) Same as (b) but for dimensionless rolling speed U_x instead of U_y. (e)/(f) are the same as (b)/(c), but for t_{exp} = 90 s instead of $t_{exp} = 59.22$ s. (d) The difference between standard deviation and mean of U_x and U_y is plotted against t_{exp}. The mean and the standard deviation of U_x simply increase with increasing measurement time. This is due to the fact that propellers to the left of the field of view can reach the field of view more easily if they are rolling faster. The mean of U_y stays constant at zero, due to symmetry reasons (the field of view is in the middle of the capillary). The standard deviation of U_y first increases with t_{exp} since faster propellers below and above the field of view can reach the field of view during the measurement time more easily if they are faster. For large t_{exp} this effect is countered by the depletion of propellers above and below the field of view and the additional effect that propellers to the left of the field of view can reach the field of view more easily if they have low U_y.

6. Discrete optimization during 3D reconstruction.

The optimal offset parameters were found in a stepwise fashion. What needed to be optimized were eight translatory shift parameters (zero for the first projection, two for the four remaining projections each). The eight translatory shift parameters were first varied in steps of p_1 pixels. The shift parameters that maximized the number of voxels that were passed by all five projections were subsequently varied in steps of $p_i < p_{i-1}$ pixels. This was repeated until the final step size of 1 pixel was reached. Values for p_1 were typically chosen between 3 and 5, depending on the size of the propeller to be reconstructed. The number of optimization rounds varied between three and five, also depending on the propeller size. This optimization procedure should always find the global optimum, if the objective function is convex and if the start conditions are close enough to the global optimum so that it can be reached (i.e. closer than the sum of the p_i). For a multi-peaked objective function the found optimum does not necessarily correspond to the global optimum (Figure S5).

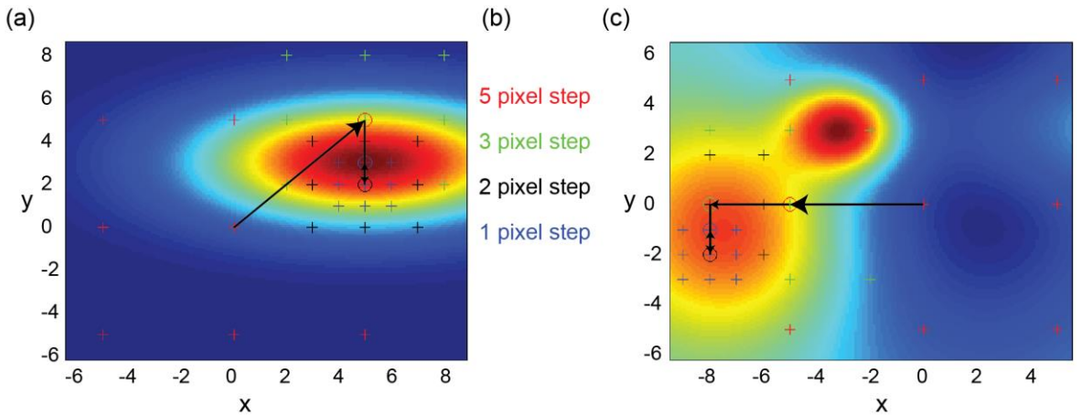

Figure S5: (a) The discrete optimization algorithm at work in the simple case of a convex objective function and only two variables (x and y). The color code for the four optimization steps is denoted in panel (b). Both x and y are varied by the step size. The best value (marked by circle) is the start position for the next optimization step. The progression to the found optimal value is marked by black arrows. For a convex objective function, the algorithm should always find the global optimum provided it is not too far away (i.e. smaller than the sum of the p_i) from the initial values (x=0, y=0). (c) For a multi-peaked objective function, the found optimal value may not correspond to the global optimum.

7. Geometric parameter extraction.

Based on the reconstructed 3D shapes of propellers (see main text), nine geometric parameters $(V, l_{\max}, O, H, I, \gamma, \chi, \Psi, S)$ were extracted. (X, Y, Z) are the coordinates of voxels, where Z is an axis parallel to the axis around which the structure rotated in experiments. The mean of the voxel coordinates (center of mass of the shape) is equal to the origin of the coordinate system. The geometric parameters volume V, maximum voxel distance $l_{\max}$ and surface area O were calculated based on the voxels that define the shape. The surface area was defined by the number of exposed voxel faces. The surface roughness (due to cubic voxels) increased the surface area somewhat. This could be seen when calculating the sphericity of a sphere approximated with voxels, which approached a value of about 0.68 instead of 1 as expected for an actual sphere.

The handedness parameter is defined as

$$H = \sum_{\mathrm{i}=\min Z}^{(\max Z)-1} \frac{(\vartheta_{i+1} - \vartheta_i)}{4V} \frac{(r_{i+1} + r_i)(a_{i+1} + a_i)}{n}, \tag{S5}$$

where ϑ is the azimuthal angle and r the radius of the mean coordinate of an X, Y section (at $Z = i$) with area a. n is the number of X, Y sections. The handedness parameter thus measures the degree to which the angle ϑ changes between Z-sections. The change in ϑ is weighted by the mean radius, since small shape changes can lead to large changes in ϑ if r is close to zero. Furthermore, the change in ϑ is multiplied by the mean area a and divided by V in order to make H dimensionless. Figure S6 a provides a schematic explanation of the handedness parameter.

The inertia parameter is defined similarly as

$$I = \sum_{\mathrm{i}=\min Z}^{\max Z} r^2 \tag{S6}$$

where r is again the radius of the mean coordinate of a X, Y section (at $Z = i$).

The average width to length ratio is defined as:

$$\gamma = \sum_{\mathrm{i}=\min Z}^{\max Z} \frac{\langle r_b \rangle}{(\max Z - \min Z)n}, \tag{S7}$$

where $\langle r_b \rangle$ is the mean radius (in polar coordinates) of voxels on the boundary of a X, Y section (at $Z = i$). n is the number of X, Y sections. γ will be small for structures elongated parallel to the axis of rotation and large for structures elongated perpendicular to the axis of rotation. A schematic illustration of the parameter γ is given in Figure S6 b.

The chirality is defined as

$$\chi = \min \frac{V(A \cup A') - V(A \cap A')}{V(A)}, \tag{S8}$$

where A defines the reconstructed shape and A' its mirror image[18]. $V(\dots)$ denotes the volume of a shape. Theoretically, χ needs to be minimized over all three rotational and all three translational degrees of freedom and is thus independent of the axis of rotation of the propeller. Therefore, we introduced the pseudo-chirality, where the minimization is simplified by centering both A and A' at the origin and varying only the angle around which the propeller rotated in the experiment. Due to this simplification the computed chirality measures can reach values above 1, although the chirality as defined above takes values between 0 and 1[18]. A schematic explanation (2D case) of the chirality can be found in Figure S6 d.

The sphericity is defined as $\Psi = \frac{\pi^{\frac{1}{3}}(6V)^{\frac{2}{3}}}{O}$. It is one for a sphere and smaller than one for any other shape.

The spikyness measure is defined as $S = V^{-\frac{1}{3}} \sqrt{\sum(X^2 + Y^2 + Z^2)}$. S is minimal for a solid sphere and maximal for a hollow sphere. S will generally be higher if the structure is elongated in one direction or several directions (spikes).

In total, 9 geometric parameters ($V, l_{\max}, O, H, I, \gamma, \chi, \Psi, S$) were extracted. The dimensional parameters ($V, l_{\max}, O, I$) have dimensions of µm, µm^2 or µm^3.

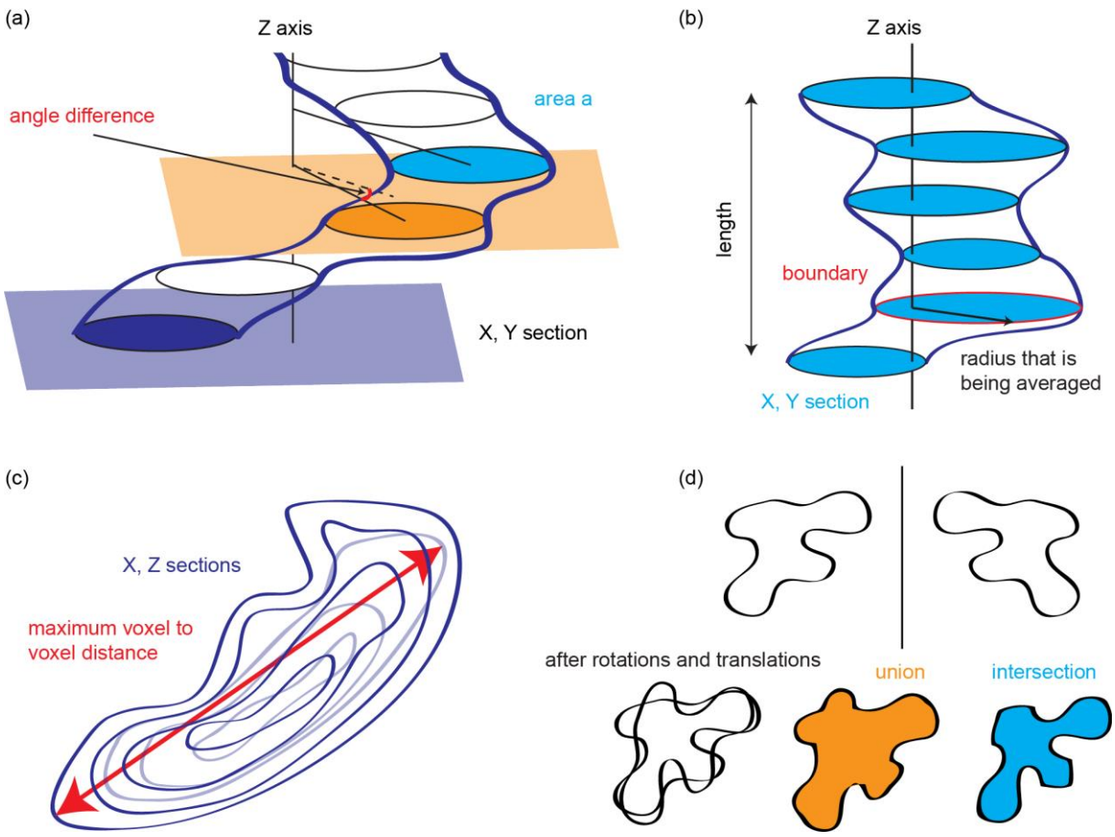

Figure S6: Explanatory schematics for selected geometric parameters. The axis of rotation is the Z axis. (a) The handedness parameter H is calculated based on angle differences between consecutive X, Y sections. The dashed line indicates the projection of the line connecting the Z axis and the mean voxel position in the blue X, Y section onto the previous orange X, Y section. The angle between the dashed line and the solid line in the orange X, Y section is the angle difference $(\vartheta_{i+1} - \vartheta_i)$ in equation 4. (b) The average width to length parameter γ is calculated based on the average over the mean radial values r_b of voxels at the boundary of one X, Y section. The boundary is indicated in red and the black arrow indicates r_b. (c) The maximum voxel to voxel distance $l_{\max}$ is indicated by the red arrow. The direction of $l_{\max}$ is in general not parallel to X, Y or Z. (d) The chirality parameter χ is illustrated for the 2D case. The black outlined shapes are mirror images of each other. By rotation and translation these can be made to overlap. The union is indicated in orange and the intersection in blue. Based on these, a preliminary chirality parameter $\hat{\chi}$ can be calculated. The shapes now need to be further rotated and translated in order to find the minimal value of $\hat{\chi}$, which is χ.

8. Artificial shapes created by a random process.

To test whether the synthesized shapes are random, the distributions of the geometric parameters were compared to those of random shapes (see Figure 1), which were generated in the following way. First, a sphere of radius $r_0 = 20 \times \xi_1 + 2$ is placed in the origin ($\mathbf{x}_0 = (0,0,0)$) of an orthogonal coordinate system (x, y, z). Here, ξ_i are random variables drawn from the uniform distribution on $[0,1]$. Then new spheres are added at positions $\mathbf{x}_i = \mathbf{x}_{i-1} + 40\,(\xi_2, \xi_3, \xi_4) - 20\,(1,1,1)$ in a stepwise manner. The process of adding spheres is continued while $\xi_5 < t$ (and at least until 2 spheres were added), where t is a threshold parameter that starts at 0.001 and is increased by 0.001 in every step. The radii of new spheres are chosen so that they just touch the nearest sphere, which is not necessarily the latest created. If the new radius was larger than 5 voxels, the new sphere would be added to the shape. Otherwise the algorithm proceeds to the next sphere addition step, without adding a sphere in this step. Examples of shapes created by the described random process are displayed in Figure S7.

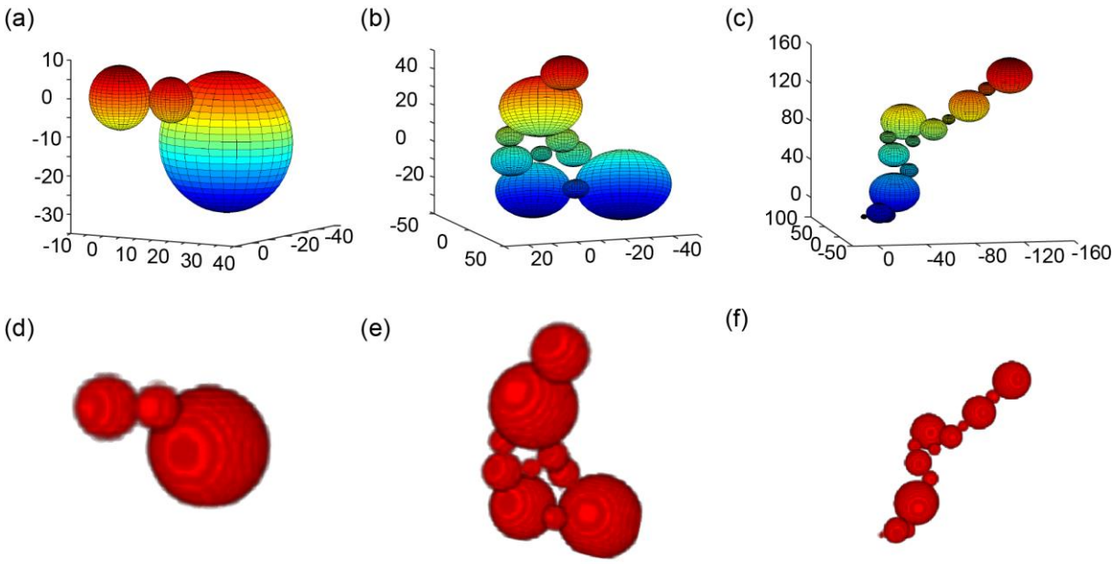

Figure S7: Examples of artificial shapes from a random process. (a-c) Visualization of shapes based on sphere center positions and radii. (e-f) The same shapes are visualized again after approximating the spheres by voxels and saving them in the same format as the reconstructed 3D shapes.

9. Test whether measurement close to a glass interface interferes with speed measurement.

The speed measurements on which the reported dimensionless speed values are based, were done close to a glass interface. Propulsion speeds measured in this way might be different from the propulsion speeds that would have been observed if the structure had been actuated in bulk liquid. To test whether the presence of a glass interface influences the propulsion, we conducted the following experiment: The motion of a propeller structure actuated by a rotating field of 30 Hz was recorded far from a surface (in bulk water) and at the lower surface of a capillary. Figure S8 shows the trajectories of the propellers during a time period of 7.33 seconds. It can be seen that the directions of motion, as well as the speed of the propeller is different. In the bulk, the structure propels (moving perpendicular to the plane in which the actuating field is rotating) with a speed of about 5.1 µm s^{-1}. The "rolling" speed of 0.5 µm s^{-1} is negligible in this case and probably due to diffusion. Close to the glass surface the structure propels with a speed of 3.5 µm s^{-1} and rolls with a speed of 4.1 µm s^{-1}. Based on optical images, no differences in the shape of the propeller can be discerned in the two videos, indicating that the propeller shape probably remained unchanged when switching from the bulk to the surface measurement. The difference in the measured propulsion speed indicates that the propulsion speed can be influenced by the presence of a surface. Indeed we previously used speed measurements in bulk liquid, to accurately measure the dependence of the propulsion speed on the actuating frequency[1]. However, in order to ensure that the measured dimensionless speeds can be compared to previously published values for designed propellers,

we measured the speeds close to a glass surface, following the methodology used throughout the literature.

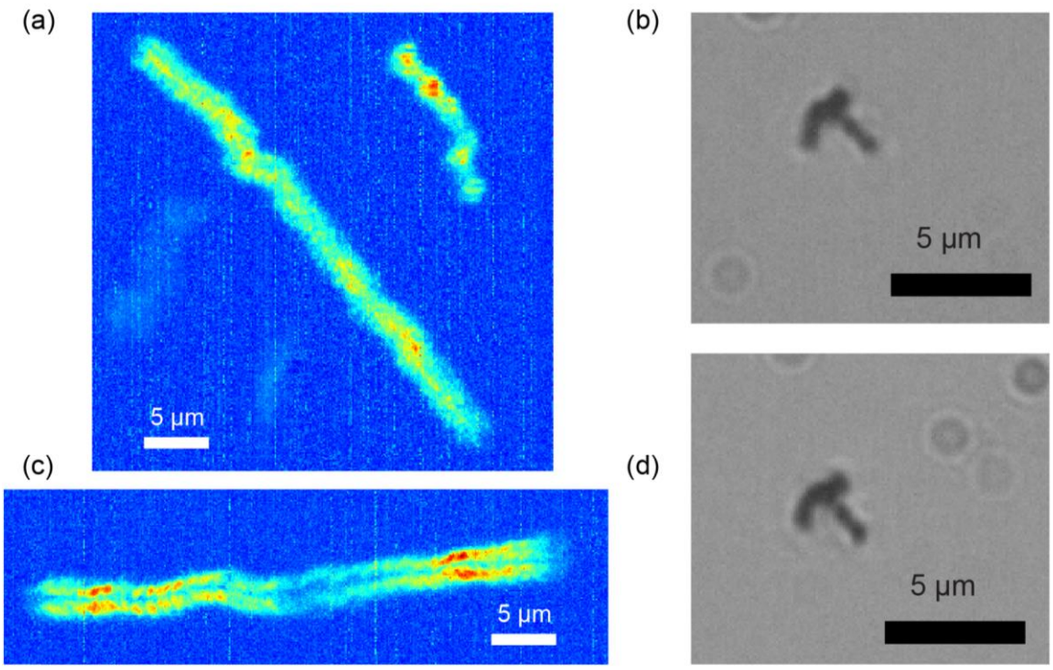

Figure S8: Comparison of movement of magnetically actuated structure in bulk water and close to a surface. (a)The structure is actuated by a 2 mT, 30 Hz rotating magnetic field close to the lower capillary surface. The trajectory is visualized during a time period of 7.33 s. The second, shorter trajectory in the upper right corner stems from another structure in the field of view, which is not of interest here. (b) Video microscopy image of the actuated magnetic structure, taken from the video where the structure is actuated close to the surface. (c)The same structure being actuated by the same external magnetic field in bulk water, far away from a surface. Again the trajectory is visualized during a time period of 7.33 s. (d) Video microscopy image of the actuated magnetic structure, taken from the video where the structure is actuated in bulk water.

10. Determination of the axis of rotation

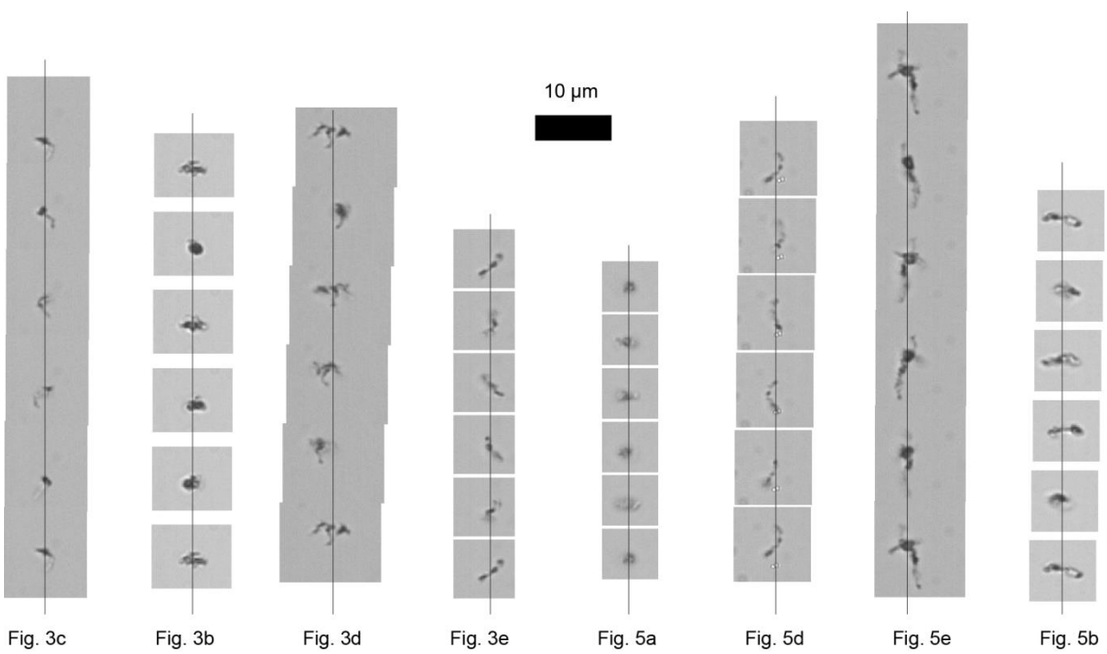

Figure S9: Determination of the rotation axes for the propellers displayed in the main text. Six consecutive projections of the microstructures are arranged in a way so that the propeller movement due to rolling is removed. The axis of rotation is vertical and the horizontal position needs to be determined. Ideally a particular feature, lying on the propeller axis, is identifiable in all six projections. This feature will lie on a vertical line, thus indicating the propeller axis. In principle, the horizontal positions of the rotation axis can then be used to determine the axis of rotation in 3D. In order to visualize the axis of rotation in the (2D) renderings of the 3D geometries displayed in the main text, prominent propeller features were used to indicate the approximate position of the axis of rotation. The scale is the same in all images and indicated by the scale bar above.

11. Distribution of rolling speeds

Besides the propulsion speed v_y we also measured the rolling speed for randomly shaped magnetic microstructures. We investigated with which geometric parameters the rolling speed might correlate, by calculating the Pearson correlation coefficient for every multiplicative combination of extracted geometric parameters and measured variables with the right units of μms^{-1}. The strongest correlation is plotted Figure S10a. The observation that the rolling speed increases with frequency and a length scale (V/O), might be ultimately grounded in the linearity of the Stokes equations for Newtonian fluids. This motivated us to define a dimensionless rolling speed U_x analogously to the dimensionless propulsion speed used in the main text. A histogram of the dimensionless rolling speed is displayed in Figure S10b. The rolling speed (as well as the dimensionless rolling speed, see Figure S10c) increases with spikyness (S) and the average width to length ratio (γ), suggesting that objects elongated perpendicular to the axis of rotation make good rollers. Previous experimental realizations of rollers also used rodlike structures rotating around their short axis[19-23]. Why this might increase the rolling speed could be investigated in future theoretical studies.

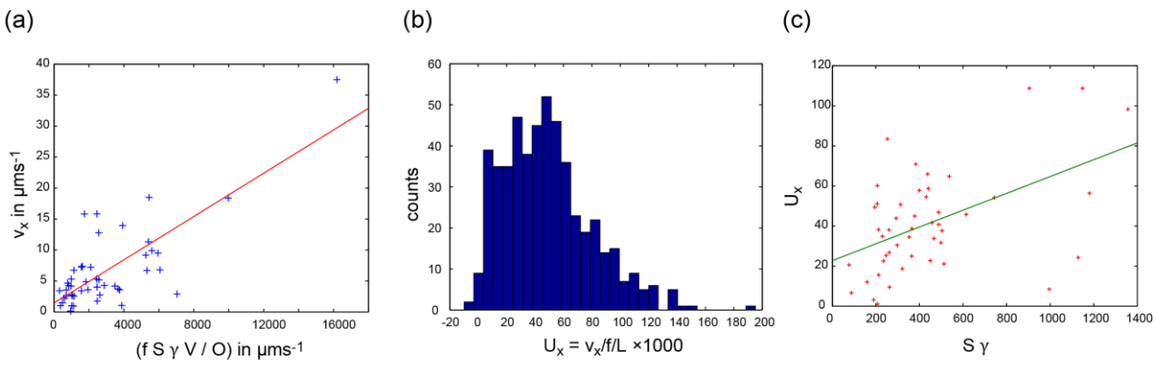

Figure S10: (a) The rolling speed v_x is plotted against the multiplicative combination of geometric parameters (with units of μms^{-1}, and using every parameter at most once), with which it correlated strongest as measured by the Pearson correlation coefficient (0.77). (b) A histogram of a dimensionless rolling speed, defined equivalently to the

dimensionless propulsion speed used in the main text. (c) The dimensionless rolling speed also correlates with the spikyness parameter S and the average width to length ratio γ (Pearson correlation coefficient 0.50).

12. Description of the supporting videos

Video 1: Video showing the movement of the propeller depicted in Figure 3c. The video is slowed down fourfold in comparison to real time. The propeller is rotating with 40 Hz. Horizontal motion (left to right) is rolling, whereas vertical motion is swimming. The video frame size corresponds to an area of 22 (width) by 49 (height) micrometers in real space.

Video 2: Video showing the movement of the propeller depicted in Figure 3d. The video is slowed down fourfold in comparison to real time. The propeller is rotating with 40 Hz. Horizontal motion (left to right) is rolling, whereas vertical motion is swimming. The video frame size corresponds to an area of 83.3 (width) by 46.9 (height) micrometers in real space.

Video 3: Video showing the movement of the propeller depicted in Figure 3e. The video is slowed down fourfold in comparison to real time. The propeller is rotating with 40 Hz. Horizontal motion (left to right) is rolling, whereas vertical motion is swimming. The video frame size corresponds to an area of 21 (width) by 37.8 (height) micrometers in real space.

13. Author contributions

The study was designed by D.F. and P.J.V. Experiments and data analysis were performed by P.J.V. D.F. supervised the work. D.F., P.F., S.K. and P.J.V. discussed the results and commented the manuscript that was drafted by P.J.V.

Supporting References

1 Vach, P.J.; Brun, N.; Bennet, M.; Bertinetti, L.; Widdrat, M.; Baumgartner, J.; Klumpp, S.; Fratzl, P.; Faivre, D. *Nano Lett.* **2013**, 13, 5373-5378.

2 Cui, X.; Antonietti, M.; Yu, S. H. *Small* **2006**, 2, 756-759.

3 Zhang, Z.; Duan, H.; Li, S.; Lin, Y. *Langmuir* **2010**, 26, 6676-6680.

4 Zhang, W.-M.; Wu, X.-L.; Hu, J.-S.; Guo, Y.-G.; Wan, L.-J. *Adv. Funct. Mater.* **2008**, 18, 3941-3946.

5 Zhang, L.; Abbott, J. J.; Dong, L.; Peyer, K. E.; Kratochvil, B. E.; Zhang, H.; Bergeles, C.; Nelson, B. J. *Nano Lett.* **2009,** 9, (10), 3663-3667.

6 Ghosh, A.; Fischer, P. *Nano Lett.* **2009,** 9, (6), 2243-2245.

7 Tottori, S.; Zhang, L.; Qiu, F.; Krawczyk, K. K.; Franco-Obregón, A.; Nelson, B. J. *Adv. Mater.* **2012,** 24, (6), 811-816.

8 Pak, O. S.; Gao, W.; Wang, J.; Lauga, E. *Soft Matter* **2011,** 7, (18), 8169-8181.

9 Bennet, M.; McCarthy, A.; Fix, D.; Edwards, M.R.; Repp, F.;, Vach, P.; Dunlop, J.W.;, Sitti, M.; Buller, G.S.; Klumpp, S.; Faivre, D. *PLoS One* **2014**, 9, e101150.

10 Happel, J.; Brenner, H. *Low Reynolds number hydrodynamics: with special applications to particulate media*. Vol. 1 (Springer, 1983).

11 Li, J.; Sattayasamitsathit, S.; Dong, R.; Gao, W.; Tam, R.; Feng, X.; Ai, S.; Wang, J. *Nanoscale* **2014**, 6, 9415-9420.

12 Schamel, D.; Mark, A. G.; Gibbs, J. G.; Miksch, C.; Morozov, K. I.; Leshansky, A. M.; Fischer, P. *Acs Nano* **2014**, 8(9), 8794-8801.

13 Schuerle, S.; Pané, S.; Pellicer, E.; Sort, J.; Baró, M. D.; Nelson, B. J. *Small* **2012,** 8, (10), 1498-1502.

14 Gao, W.; Feng, X.; Pei, A.; Kane, C. R.; Tam, R.; Hennessy, C.; Wang, J. *Nano Lett.* **2013,** 14, (1), 305-310.

15 Zhang, L.; Peyer, K. E.; Petit, T.; Kratochvil, B. E.; Nelson, B. J., 2010 10th IEEE Conference on Nanotechnology (IEEE-NANO), **2010**,893-896.

16 Peters, C.; Ergeneman, O.; García, P. D. W.; Müller, M.; Pané, S.; Nelson, B. J.; Hierold, C. *Adv. Funct. Mater.* **2014**,24, (33), 5269-5276.

17 Walker, D.; Kubler, M.; Morozov, K. I.; Fischer, P.; Leshansky, A. *Nano Lett.* **2015**.

18 Petitjean, M. *Entropy* **2003,** 5, (3), 271-312.

19 Sing, C. E.; Schmid, L.; Schneider, M. F.; Franke, T.; Alexander-Katz, A. *Proc. Natl. Acad. Sci. USA* **2010***,* 107, 535-540.

20 O Mair, L.; Evans, B.; Hall, A.R.; Carpenter, J.; Shields, A.; Ford, K.; Millard, M.; Superfine, R. *J. Phys. D. Appl. Phys.* **2011**, 44, 125001.

21 Zhang, L.; Petit, T.; Peyer, K.E.; Kratochvil, B.E.; Zhang , J.; Lou, J. ; Nelson, B.J. 2010 IEEE 4th International Conference on Nano/Molecular Medicine and Engineering (NANOMED), **2010**, 38-43.

22 Zhang, L.; Petit, T.; Lu, Y.; Kratochvil, B.E.; Peyer, K.E.; Pei, R.; Lou, J.; Nelson, B.J. *Acs Nano* **2010**, 4, 6228-6234.

23 Zhang, L.; Petit, T.; Peyer, K. E.; Nelson, B. J. *Nanomed. – Nanotechnol.* ***2012***, 8, 1074-1080.